frontiers | Frontiers in Chemistry

TYPE Original Research
PUBLISHED 29 September 2022
DOI 10.3389/fchem.2022.949979

OPEN ACCESS

EDITED BY
Xingke Cai,
Shenzhen University, China

REVIEWED BY
Zhenming Xu,
Nanjing University of Aeronautics and Astronautics, China
Yongtao Li,
Anhui University of Technology, China

*CORRESPONDENCE
Wei Wang,
wangwei2017@czu.cn
Min Wang,
milladengdai@hotmail.com
Tianyu Liu,
liuty@czu.cn

SPECIALTY SECTION
This article was submitted to Electrochemistry, a section of the journal Frontiers in Chemistry

RECEIVED 22 May 2022
ACCEPTED 29 July 2022
PUBLISHED 29 September 2022

CITATION
Shen H, Zhang W, Zhang Y, Wang W, Wang M and Liu T (2022), A novel exfoliated manganese phosphoselenide as a high-performance anode material for lithium ions storage. *Front. Chem.* 10:949979. doi: 10.3389/fchem.2022.949979

A novel exfoliated manganese phosphoselenide as a high-performance anode material for lithium ions storage

Hailin Shen, Wei Zhang, Yuheng Zhang, Wei Wang*, Min Wang* and Tianyu Liu*

School of Chemical Engineering and Materials, Changzhou Institute of Technology, Changzhou, China

Layered manganese phosphoselenide ($MnPSe_3$) is expected to be a potential anode for Li ions storage due to it combines the merits of phosphorus with metal selenide. It promotes charge transfer and ensures a high theoretical capacity of up to 746 mA h g^{-1}. In this work, a comprehensive study clearly demonstrated that bulk $MnPSe_3$ electrode is the inability to maintain the integrity of the structure with severe detectable fracture or pulverization after full lithiation/delithiation, resulting in poor rate capability and cycling stability. Additionally, exfoliated few-layered $MnPSe_3$ nanoflakes by the ultrasonic method show enhanced electrical conductivity and resistance to volume expansion. It has a high initial discharge/charge capacity reaching to 524/796 mA h g^{-1} and outstanding cycling stability with charge capacities of 709 mA h g^{-1} after 100 cycles at 0.2 A g^{-1} within the potential window of 0.005–3 V vs. Li^+/Li. While further improving the cycles, the retention rate was still held at ~72% after 350 cycles. This work provides new insights into exploiting new novel layered materials, such as $MnPSe_3$ as anodes for lithium-ion batteries.

KEYWORDS

manganese phosphoselenide, exfoliation, anode, cycling stability, LIBs

Introduction

As is known, lithium-ion batteries (LIBs) (Liu et al., 2010; Dunn et al., 2011; Goodenough, 2014) have been utilized in countless commodities, such as mobile phones and electric vehicles. However, its wider applications are impeded owing to limiting materials, so there is still great potential as long as more novel electrode materials are exploited for LIBs.

So far, various metal selenides, such as $FeSe_2$ (Kong et al., 2019; Yousaf et al., 2020), MnSe(Li et al., 2016; Liu et al., 2018; Li Z. et al., 2019), and $CoSe_2$ (Yu N. et al., 2019; Xu et al., 2020) have been deeply studied as active materials in LIBs. Nevertheless, it presents the challenges of inferior rate capability and rapid capacity loss. Some researchers have also focused on phosphorus-based materials such as black phosphorus (Dahbi et al., 2016; Del Rio Castillo et al., 2018), SiP (Duveau et al., 2016), FeP (Jiang et al., 2017), and GeP (Li

W. et al., 2019; Li X. et al., 2019; Fan et al., 2019), which also exhibits the inferior cycling performance. Nevertheless, improving the electrochemical performance of metal sulfides and phosphides in terms of rate capability and cycling stability is an enormous challenge due to the large volume change that can lead to crushing and loss of electrical contact.

Recently, a novel ternary metal phosphide sulfide/selenides (MPX_3, M is transition metal, such as Mn, Zn, *etc*; X is Se or S (Brec, 1986; Pei et al., 2018; Gusmao et al., 2019; Samal et al., 2021), have been investigated in electrocatalysis (Byvik et al., 1982; Dedkov et al., 2020), hydrogen storage (Cabria and El-Meligi, 2018) and toxicological hazards (Latiff et al., 2018). However, the MPX_3 empolyed as active materials in LIBs are rarely reported. The layered MPX_3 owns attractive lithium storage ability for rechargeable ion batteries. Its unique two-dimensional (2D) layered nanostructure, which is composed of weak van der Waals stacking between layers, is deemed to be an ideal framework for fast Li^+ storage. The layered structure alleviates the volume stress, generates abundant ion diffusion pathways and speedy electron transportation owing to lower energy barrier (Fan et al., 2019; Ding et al., 2020). More importantly, the preferred bandgaps\ of MPX_3 (1.3–3.5 eV) (Wang et al., 2018) and potential ionic conductivity make MPX_3 as superior anode electrode materials. Some groups have reported like-MPX_3, such as $MnPS_3$ (Sang et al., 2020), $CoPS_3$ (Jana et al., 2020), $FePSe_3$ (Xing et al., 2020), $NiPS_3$ (Dangol et al., 2018) and $SnPSe_3$ (Ren et al., 2020), exhibit a promising performance of lithium/sodium ions storage.

The manganese phosphorous selenide ($MnPSe_3$) is one of MPX_3, isostructural with $FePSe_3$. The $MnPSe_3$ possesses an interlayer spacing of~0.32 nm (Li et al., 2014), much larger than the diameter of Li^+ (~0.152 nm), providing channels for Li^+ diffusion in the insertion/extraction process. $MnPSe_3$ as anodes also have a high theoretical capacity of 746 mA h g^{-1} by forming Li_3P and Li_2Se alloy (Li et al., 2013; Gusmão et al., 2019; Tang et al., 2020). However, the numerous overlapping layers of bulk $MnPSe_3$ lead to a decreasing active surface area, slow charge transfer, and even poor resistance to volume expansion in lithiation/delithiation. According to previous studies (Abdelkader and Kinloch, 2016; Chen et al., 2016; Shen et al., 2020), mechanical exfoliation can effectively narrow the size and thickness of bulk materials, causing abundant exposed active sites, highly tunable morphology, reduced diffusion length of charge carriers for Li^+ and perfect resistance to volume change.

In this work, the lithiation/delithiation processing of bulk $MnPSe_3$ as the anode in LIBs has been disclosed by half-cell. It occurs to serious volume expansion/contraction for bulk $MnPSe_3$ in lithiation/delithiation, even the tracking $MnPSe_3$ electrode is unable to maintain high integrity with serious cracks or pulverization. Thus, we reduced bulk $MnPSe_3$ to a few layered $MnPSe_3$ nanoflakes by mechanical exfoliation and comprehensively compared the storage Li^+ performances of exfoliated $MnPSe_3$ to that by grinding as LIBs anodes. Moreover, the exfoliated $MnPSe_3$ electrode shows an initial discharge/charge capacity of 524/796 mA h g^{-1}, and a retention rate of 88% and 72% after 100 and 350 cycles, respectively at 0.2 A g^{-1}. The improved resistance to expansion and pulverization and rapid reaction kinetics indicate the exfoliated $MnPSe_3$ is able to achieve superb cyclic stability. Ultimately, exfoliated $MnPSe_3$ is considered a great dynamism and potential anode material with predominant performance in LIBs.

Experimental section

Synthesis of bulk and exfoliated $MnPSe_3$

All chemicals are available without further treatment. The bulk $MnPSe_3$ is prepared by grinding in the agate mortar for about 30 min. The thinner and smaller $MnPSe_3$ nanoflakes continue to be processed by ultrasonic exfoliation (Zhang et al., 2016). These bulk particles (100 mg) are reduced to thinner by ultrasonic (1000 W, 4 h) in N-Methyl pyrrolidone (NMP) solvent (150 ml) and centrifugation (3,000 rpm for 20 min) to remove large particles. Then the small-size nanoflakes were obtained by washing and drying in a vacuum oven.

Preparation of $MnPSe_3$ electrodes and the coin-type half-cell for LIBs

The slurry of the $MnPSe_3$ electrode was prepared by mixing 70 wt% $MnPSe_3$ nanoflakes and 20 wt% carbon nanotubes (CNTs) and 10 wt% carboxymethyl cellulose (CMC), which was spread evenly on a copper foil (load of 1.5–2.0 mg cm^{-1}), then the obtained products were cut into a disc (diameter of 10 mm) and dried at 70°C for about 12 h under vacuum. The surface morphology of $MnPSe_3$/CNT/CMC electrode is shown in Supplementary Figure S1, exhibiting the $MnPSe_3$ nanoflakes embedded in the uniform carbon nanotubes matrix. The carbon nanotubes are able to promote a quick electron/ion transfer and alleviate volume stress. Lithium metal foil, polypropylene (PP), and $MnPSe_3$/CNT/CMC electrode sequentially were put into the CR2032 cell case for assembling sequentially in the glove box. The electrolyte is composed of 1 M $LiPF_6$ dissolved in EC/DMC/DEC (1/1/1 v/v/v) mixed solution.

Electrochemical measurements of $MnPSe_3$ anode

The galvanostatic charge/discharge, rate performance, and cycle performance of half-cell were performed in the

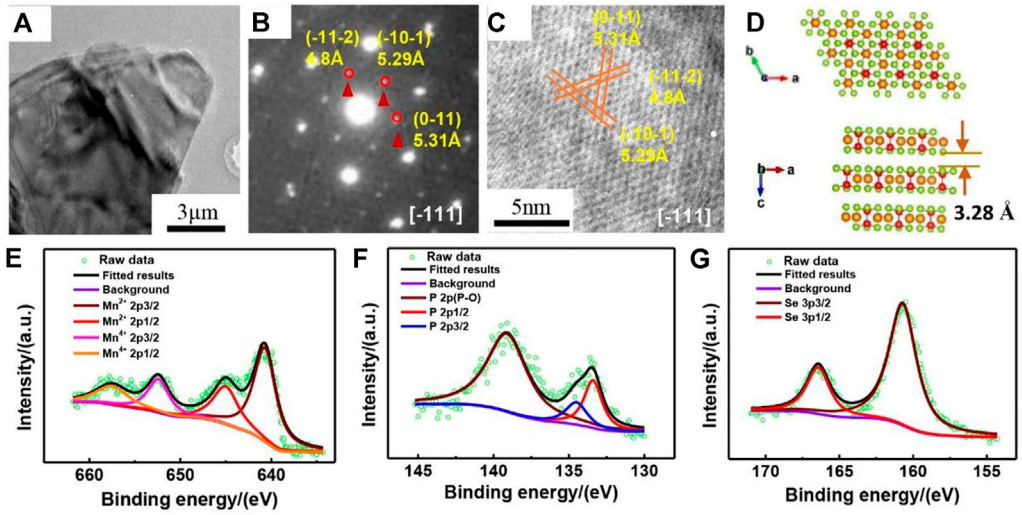

FIGURE 1
The purity, structure, and composition of $MnPSe_3$ nanoflake. **(A)** The typical TEM image of layered $MnPSe_3$. **(B)** The selected area electron diffraction (SAED) pattern of $MnPSe_3$ nanoflake view from [-111]. **(C)** The high-resolution TEM (HRTEM) image of $MnPSe_3$ was viewed along the same direction corresponding to the SAED. **(D)** The crystal structure schematic of $MnPSe_3$ along the b and c axes, respectively. **(E–G)** The high-resolution XPS shows spectra of the Mn, P, and Se elements, respectively.

volt range from 0.005 to 3 V (vs. Li^+/Li). Cyclic voltammograms (CVs) were tested using an electrochemical working station in the voltage range of 0.005–3.0 V (vs. Li^+/Li) at 0.05 mV s^{-1}. Electrochemical impedance spectroscopy (EIS) was conducted in a frequency range of 10 K to 0.1 HZ in the same test system.

Material test and characterization instruments

Battery testing system (a Land CT 2001A, WuHan, China). Electrochemical working station (a 1,400 Cell Test system, Solartron, China). X-ray diffractometer (XRD-Bruker D2, Cu K radiation, λ = 1.5418 Å). A field-emission scanning electron microscopy (SEM, Hitachi-S4800). High-resolution transmission electron microscopy (TEM, JEM 2100, JEOL, Japan, 200 kV). X-ray photoelectron spectroscopy (XPS, ThermoFisher EscaLab 250Xi).

Results and discussion

As clearly displayed by the low-magnification TEM in Figure 1A. $MnPSe_3$ exhibits an ultrathin and transparent lamellar appearance with several micrometers in plane and nanometers in thickness. The typical SAED pattern of $MnPSe_3$ show the diffraction spots of (-11-2), (-10-1), (0-11) plane with corresponding d-spacings of 4.8, 5.29, and 5.31 Å, respectively viewed along [-111] in Figure 1B, which is commensurate to HRTEM along [-111] in Figure 1C. It indicates that the as-prepared $MnPSe_3$ possesses high crystallinity and phase purity.

The schematic images of layered $MnPSe_3$ viewed from the b and c axes are shown in Figure 1D. $MnPSe_3$ belongs to a hexagonal with the lattice parameters of a = 6.387 Å, b = 6.387 Å, c = 19.996Å; and the angle α, β is 90°, γ is 107.35°. As depicted in Figure 1A, a single layer is composed of the Mn atom's central shell and the other two shells in PS_3 units. The selenide atoms are located on the two external surfaces of a $MnPSe_3$ layer (Li et al., 2014; Pei et al., 2018). Moreover, the spacing of two adjacent $MnPSe_3$ layers is 3.2 Å by Van der Waals (Li et al., 2014), which provides channels and buffers volume expansion/contraction for Li^+ insertion/extraction.

The chemical compositions of $MnPSe_3$ nanoflakes were further investigated by XPS in Figures 1E–G. As revealed by the Mn 2p spectrum, the high-resolution Mn 2p profile can be mainly fitted at 640.7 eV (2p3/2) and 651.3 eV (2p1/2), ascribed to the binding energy of Mn^{2+}, while the peaks at 642.3 eV (2p3/2) and 657.6 eV (2p1/2) indicate the presence of Mn^{4+} (Sang et al., 2020). The narrowly scanned XPS spectrum of P 2p can be contributed to double peaks at 134.5 and 133.4 eV, which are in line with the P 2p3/2 and P 2p1/2, respectively (Edison et al., 2018; Fan et al., 2019). Additionally, there are only a pair of peaks at 166.4 eV (2p3/2) and 160.7 eV (2p1/2) for the Se 2p (Gusmão et al., 2017; Dedkov et al., 2020), indicating only one form of selenium existed in the $MnPSe_3$, in agreement with aforementioned results.

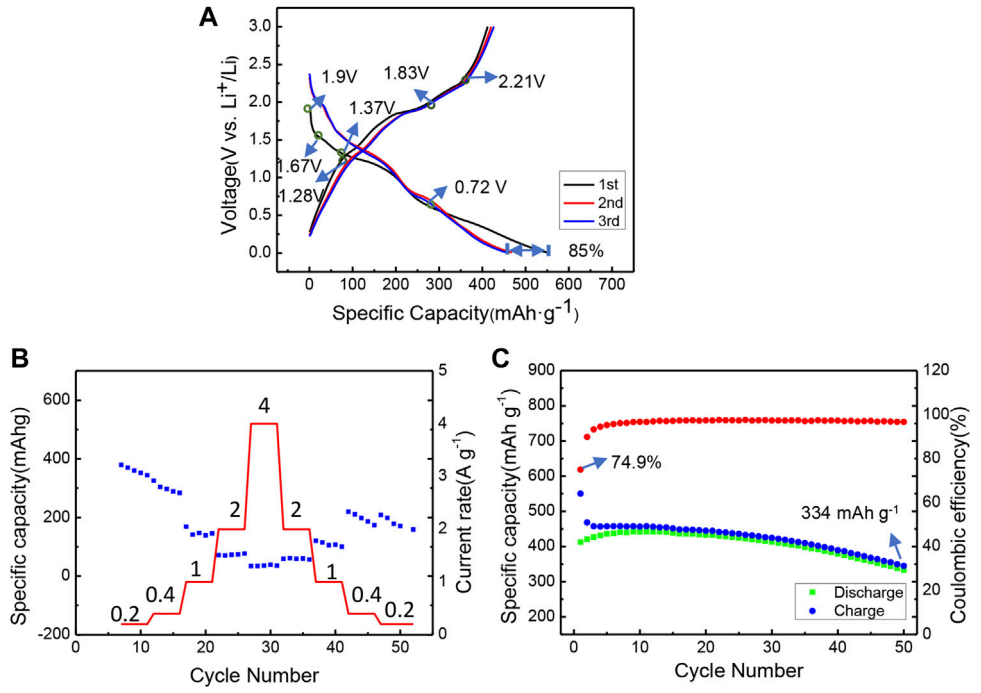

FIGURE 2
Electrochemical performance of bulk $MnPSe_3$ within the window 0.005–3 V (vs. Li^+/Li). **(A)** The initial three discharging/charging curves of $MnPSe_3$ electrode at 0.2 A g^{-1}. **(B)** The rate performance at different current densities from 0.2 to 4 A g^{-1}. **(C)** The cycling performance of $MnPSe_3$ electrode at 0.2 A g^{-1}.

Electrochemical behaviors of bulk $MnPSe_3$ have been tested in Figure 2. There are mainly four obvious plateau regions at 2.0–1.8 V, 1.75–1.58 V, 1.53–1.15 V, and 0.75–0.35 V in the first discharge curve, while the charge profile also shows three corresponding three plateaus at 2.07–2.34 V, 1.71–1.94 V, and 1.1–1.38 V, respectively in Figure 2A. Significantly, the bulk $MnPSe_3$ electrode illustrates the rate capabilities of 0.2, 0.4, 1, 2, and 4 A g^{-1}in Figure 2B. With the increase of current density, the specific capacities decay obviously for the $MnPSe_3$ electrode. When the current density reaches up to 4 A g^{-1}, the reversible capacity of 35 mA h g^{-1} is just left. The bulk $MnPSe_3$ delivers a first 412/550 mA h g^{-1} discharge/charge capacity with ~75% initial Coulombic efficiency in a potential of 0.005–3 V at 0.2 A g^{-1}, and an extremely obvious downward trend with a retained capacity of 344 mA h g^{-1} after 50 cycles in Figure 2C. It indicates the cycling durability for the bulk electrode is really poor. The bulk $MnPSe_3$ electrode possesses an inferior rate capability and more unstable cycling performance.

In order to further improve the Li^+ storage performance of $MnPSe_3$, the bulk $MnPSe_3$ was refined to nanoflakes by mechanical exfoliation. We compare the morphology between bulk $MnPSe_3$ and exfoliated $MnPSe_3$ by SEM in Figures 3A, B; Supplementary Figure S2. Compared to bulk $MnPSe_3$, exfoliated $MnPSe_3$ nanoflakes display a smaller and more uniform size. As shown in Figures 3C,D, the size distribution of $MnPSe_3$ nanoflakes was measured by particle size analysis. The size of bulk $MnPSe_3$ by hand grinding reaches ~1.2 μm. However, exfoliated $MnPSe_3$ nanoflakes have been largely narrowed to tens of nanometers. Moreover, exfoliated $MnPSe_3$ electrode exhibits more remarkable electrical conductivity than bulk $MnPSe_3$ in Supplementary Figure S3. According to reported articles (Chen et al., 2016; Dangol et al., 2018; Yu Z. et al., 2019), reducing the size and thinning the thickness of bulk 2D materials can effectively improve abundant exposed active sites and resistance to expansion/shrinkage and shortened diffusion length of charge carriers for Li ions and in the process of Li^+ insertion and extraction. In addition, as shown in Figure 3E, $MnPSe_3$ nanoflakes were prepared by two-step method. The liquid-phase ultrasonic exfoliation does not involve in phase transformation and any new phases formation. In addition, this method achieves controllable size nanoflakes and high repeatability. The obtained $MnPSe_3$ nanoflakes exhibits further enhancement on fast chargeability and long cyclability of Li^+ storage. Firstly, bulk $MnPSe_3$ were crumbled roughly by ultrasonic stripping. Secondly, smaller $MnPSe_3$ nanoflakes effectively were separated by fractional centrifugation.

Furthermore, we examined the discrepancy of the bulk and exfoliation $MnPSe^3$ in morphology and EIS, respectively in Figure 4. The side surface of exfoliated $MnPSe^3$/CNT/CMC electrode shows

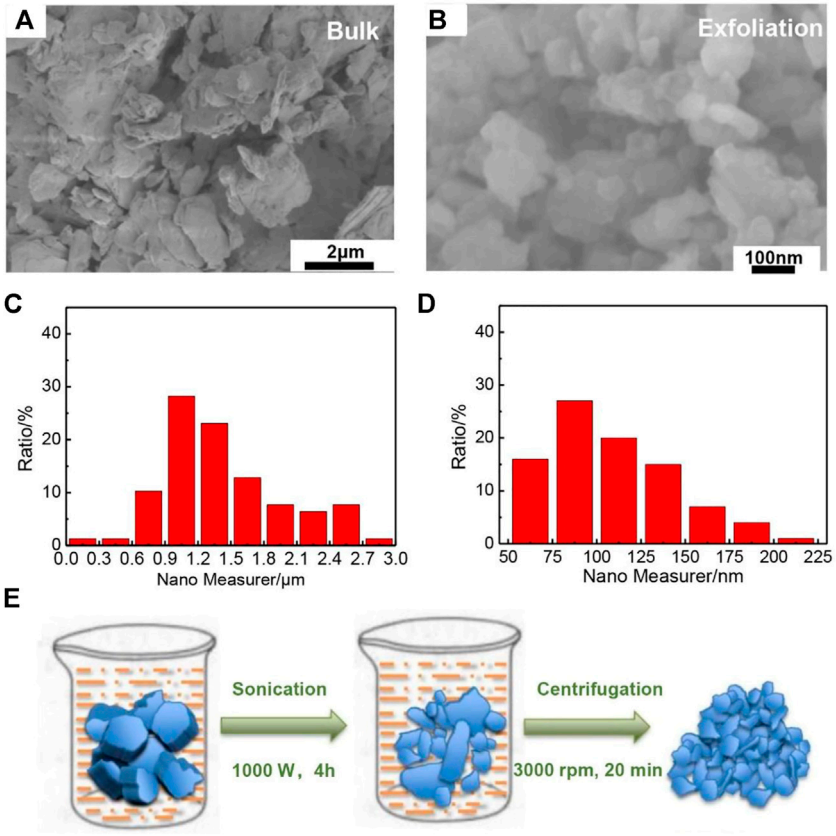

FIGURE 3
Comparison of the morphology for bulk and exfoliated $MnPSe_3$. **(A,B)** The SEM images of $MnPSe_3$ nanoflakes by hand grinding and exfoliation. **(C,D)** The size distribution of bulk and exfoliated $MnPSe_3$ nanoflakes corresponds to Figures 3A,B. **(E)** The processing illustration of $MnPSe_3$ nanoflakes was obtained by sonication-assisted exfoliation.

serious cracking, reaching ~15 μm due to severe volume expansion/shrinkage after full lithiation/delithiation in Figures 4A,B, which is a key cause of rapid failure for bulk $MnPSe^3$ electrode. While it was found that exfoliated $MnPSe^3$ remained integrity after 100 cycles. This clearly further demonstrates that exfoliated $MnPSe^3$ electrodes resist severe volume expansion owing to possessing excellent mechanical robustness. Interestingly, after 100 charge/discharge cycles, the thinner and smaller layered $MnPSe^3$ electrode obtains a lower transfer resistance than bulk $MnPSe^3$ owing to the contact separation of electrode internal components in Figure 4C, even falling from the current collector, resulting in the decreasing of electrical conductivity and ion transport properties. Thus, the exfoliated layered $MnPSe^3$ electrode facilitates Li^+ extraction from the insertion region.

To further confirm the phase transformation of $MnPSe_3$ in lithiation/delithiation, X-Ray Diffraction (XRD) has also been performed on the $MnPSe_3$ electrode in Figure 5A. The pristine $MnPSe_3$ electrode exhibits the obvious crystallographic orientations of (003), (006), and (113), and no detectable impurities were found. The *ex-situ* XRD of the $MnPSe_3$ anode presents Li_3P peaks at about 26.6°, 33.8°, and 44.3° (Kim and Cho, 2009), and Li_2Se peaks at about 25.1° and 22.6° after the first full lithiation (Liu et al., 2020), which further verify single-crystal $MnPSe_3$ is entirely alloyed to Li_3P and Li_2Se phase. While upon full delithiation, it presents a new peak at 33.1°, which is caused by the MnSe phase (Xue and Fu, 2007). The marked peaks located at other degrees originate from electrolyte decomposition on the surface of the $MnPSe_3$ electrode, which is in good agreement with reported results about like-MPX_3. Significantly, the differential capacity profiles display excellent reversibility in a redox reaction and agree well with the *ex-situ* XRD analysis, which also presents the reduction peak at 1.95, 1.66, 1.30, and 0.6 V, could correspond to the alloying reactions of Li_xMnPSe, $Li_2Se/P/Mn$ Li_3P, and SEI, respectively. Considering the analysis above, phase transformation in first lithiation/delithiation could be summarized as follows:

After First lithiation:

$$MnPSe_3 + 9Li^+ + 9e^- \rightarrow Li_3P + Mn + 3Li_2Se \quad (1)$$

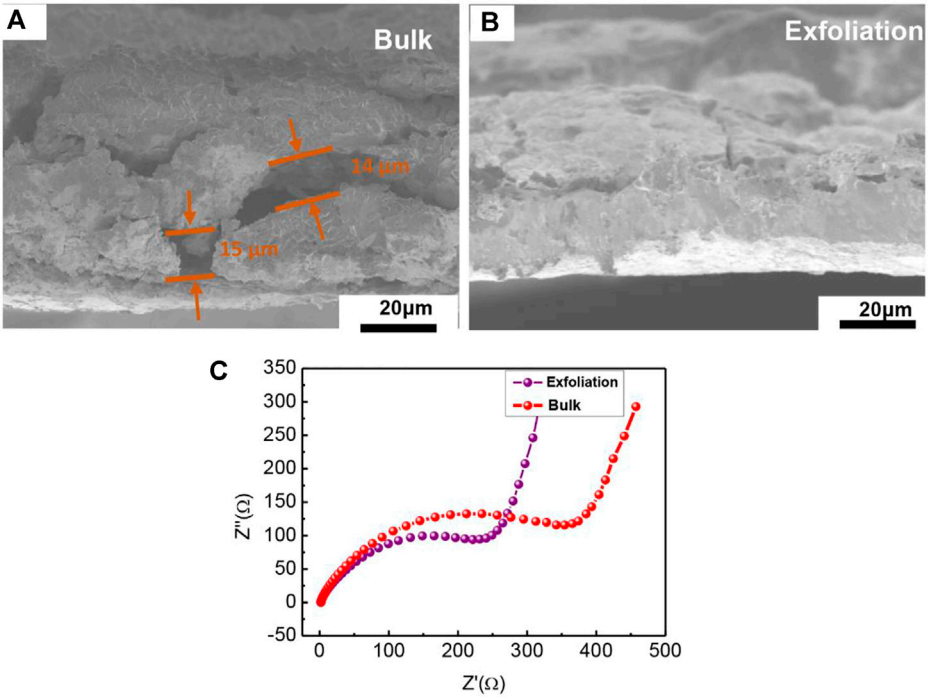

FIGURE 4
The performance analysis of $MnPSe_3$ electrode. **(A,B)** The side SEM of $MnPSe_3$ electrode before and after exfoliation in 100 charge/discharge cycles. **(C)** The impedance of $MnPSe_3$ electrode in 100 charge/discharge cycles before and after exfoliation, respectively.

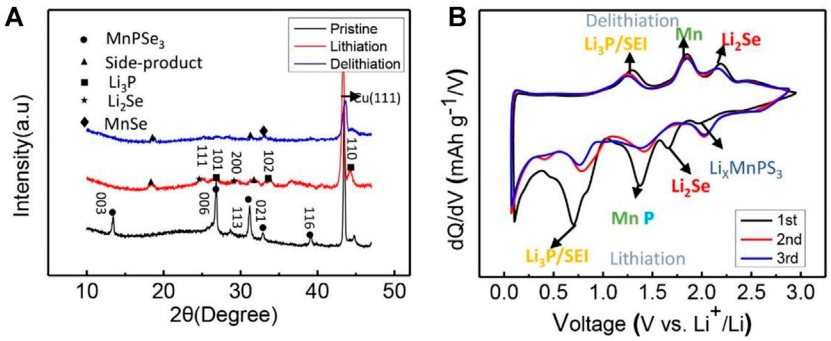

FIGURE 5
Phase characterization of $MnPSe_3$ electrode in lithiation/delithiation. **(A)** The *ex-situ* XRD patterns of $MnPSe_3$ electrodes for the first lithiation/delithiation. **(B)** The differential capacity curves of the $MnPSe_3$ electrode in the initial three cycles.

After First delithiation:

$$Li_3P + Mn + Li_2Se \rightarrow MnSe + P + 5Li^+ + 5e^- \quad (2)$$

As shown in Figure 6, the exfoliated $MnPSe_3$ anode is further utilized in a half-cell. Primarily, the typical cyclic voltammogram (CV) curves of the electrode were illustrated in Figure 6A. The initial cathodic sweep displays four distinct reduction peaks at 1.95 V, 1.6 V, 1.2 V, 0.6 V, and 0.35 V, indicating the lithiation/delithiation process is a multiple-step. The prominent peak located at 1.95 V is matched to Li_xMnPSe_3. The peaks centered at 1.6 V and 1.2 V are associated with the formation of Li_2Se, P, and Mn. The peak at 0.6 V is related to the generation of Li_3P. Another weak broad peak located at 0.35 V is attributed to the side reaction (formation of SEI film). In the following anodic sweep. The three strong peaks at 1.38 V, 2.0 V, and 2.27 V are coincident with dealloying of Li_3P, Li_2Se, and the formation of MnSe. The result above is similar to CVs profiles for like-MPX_3 ($FePSe_3$,

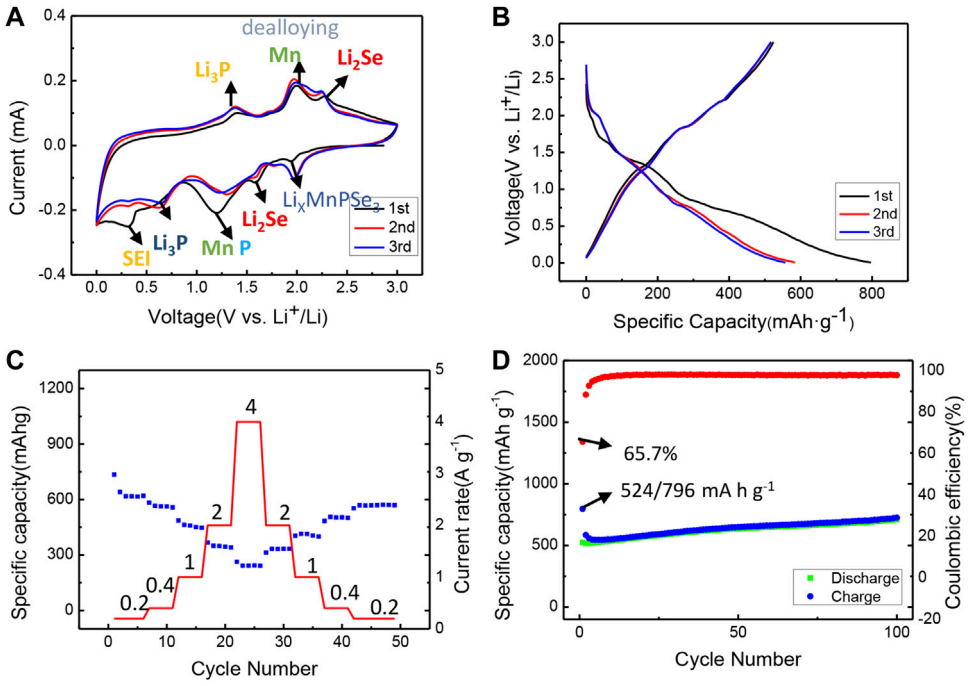

FIGURE 6
Electrochemical performance of exfoliated $MnPSe_3$ as anode in Li ions half-cell. **(A)** The CVs of the initial three cycles in the voltage window of 0.005–3 V at 0.05 mV s^{-1}. **(B)** Galvanostatic discharge/charge profiles for the first three cycles in the voltage window of 0.005–3 V (vs. Li^+/Li) at 0.2 A g^{-1}. **(C)** Rate performance of $MnPSe_3$ anode within the potential of 0.005–3 V vs. Li^+/Li at different current densities from 0.2 A g^{-1} to 4 A g^{-1}. **(D)** Cycling performance of exfoliated $MnPSe_3$ electrode tested within the potential of 0.005–3 V (vs. Li^+/Li) at 0.2 A g^{-1}.

$NiPS_3$, etc) (Sang et al., 2020; Xing et al., 2020; Liu et al., 2021). In addition, the initial three cycles curves exhibit a consistent property of reaction to that of the CV results above in Figure 6B. The charge/discharge curves and CVs in multiple cycles are also nearly overlapped, suggesting the wonderful stability of electrode.

To evaluate the lithium storage properties of the exfoliated $MnPSe_3$ at $_a$ high rate, the reversible capacities of 616, 562, 458, 348, and 242 mA h g^{-1} were obtained at current densities of 0.2, 0.4, 1, 2, and 4 A g^{-1}, respectively in Figure 6C. Moreover, the capacity achieves 331, 412, 502, and 568 mA h g^{-1} with the current density coming back to 2, 1, 0.4, and 0.2 A g^{-1}, illustrating the $MnPSe_3$ electrode maintains a remarkable rate performance. Compared to bulk MnPSe3, the cycling stability of the exfoliated $MnPSe_3$ is also effectively improved. It maintains outstanding cycling stability with capacity retention of 709 mA h g^{-1} after 100 cycles at 0.2 A g^{-1}, and capacity retention of 578 mA h g^{-1} after 350 cycles at 0.2 A g^{-1}in Figure 6D; Supplementary Figure S4.

Conclusion

In summary, this work researches on performance improvement of the $MnPSe_3$ as the anode of LIBs in detail by ultrasonic exfoliation, revealing an extraordinary ability to resist volume expansion/shrinkage in full lithiation/delithaition, which provides significant evidence for the research of like-MPX_3. The thinner and smaller $MnPSe_3$ shows superior performance to the bulk electrode material. When supplied as the anode of LIBs in half-cell, a splendid reversible capacity of 709 mA h g^{-1} was maintained for the $MnPSe_3$ within the potential window of 0.005–3 V vs. Li^+/Li after 100 cycles at 0.2 A g^{-1}. While further improving the cycles, a specific capacity of 578 mA h g^{-1} was still held after 350 cycles, which benefits from the favorable capacitance kinetics, and resist severe volume expansion. Layered $MnPSe_3$ as anode materials for LIBs meet the needs of high capacity, rapid charge-discharge, and long cycle.

Data availability statement

The original contributions presented in the study are included in the article/Supplementary Material further inquiries can be directed to the corresponding authors.

Author contributions

HS: Conceptualization (ideas; formulation or evolution of overarching research goals and aims); Experimental method

design, Performing experiments; Original draft preparation. WZ: Formal analysis. YZ: Supervision. WW: Guiding the experiment; Writing—Reviewing and Editing. MW: Resources; Investigation. TL: Writing—Reviewing and Editing.

Funding

Financial support from National Science Foundation of Changzhou Institute of Technology (YN21024).

Conflict of interest

The authors declare that the research was conducted in the absence of any commercial or financial relationships that could be construed as a potential conflict of interest.

Publisher's note

Supplementary material

The Supplementary Material for this article can be found online at: https://www.frontiersin.org/articles/10.3389/fchem.2022.949979/full#supplementary-material

References

Abdelkader, A. M., and Kinloch, I. A. (2016). Mechanochemical exfoliation of 2D crystals in deep eutectic solvents. *ACS Sustain. Chem. Eng.* 4, 4465–4472. doi:10.1021/acssuschemeng.6b01195

Brec, R. (1986). "Review on structural and chemical properties of transition metal phosphorus trisulfides MPS 3," in *Intercalation in layered materials* (Berlin, Germany: Springer), 93.

Byvik, C. E., Smith, B. T., and Reichman, B. (1982). Layered transition metal thiophosphates (MPX_3) as photoelectrodes in photoelectrochemical cells. *Sol. Energy Mater.* 7, 213–223. doi:10.1016/0165-1633(82)90085-5

Cabria, I., and El-Meligi, A. A. (2018). DFT simulation of hydrogen storage on manganese phosphorous trisulphide (MnPS3). *Int. J. Hydrogen Energy* 43, 5903–5912. doi:10.1016/j.ijhydene.2017.10.103

Chen, L., Zhou, G., Liu, Z., Ma, X., Chen, J., Zhang, Z., et al. (2016). Scalable clean exfoliation of high-quality few-layer black phosphorus for a flexible lithium ion battery. *Adv. Mat.* 28, 510–517. doi:10.1002/adma.201503678

Dahbi, M., Yabuuchi, N., Fukunishi, M., Kubota, K., Chihara, K., Tokiwa, K., et al. (2016). Black phosphorus as a high-capacity, high-capability negative electrode for sodium-ion batteries: Investigation of the electrode/electrolyte interface. *Chem. Mat.* 28, 1625–1635. doi:10.1021/acs.chemmater.5b03524

Dangol, R., Dai, Z., Chaturvedi, A., Zheng, Y., Zhang, Y., Dinh, K. N., et al. (2018). Few-layer NiPS3 nanosheets as bifunctional materials for Li-ion storage and oxygen evolution reaction. *Nanoscale* 10, 4890–4896. doi:10.1039/c7nr08745d

Dedkov, Y., Yan, M., and Voloshina, E. (2020). To the synthesis and characterization of layered metal phosphorus triselenides proposed for electrochemical sensing and energy applications. *Chem. Phys. Lett.* 754, 137627. doi:10.1016/j.cplett.2020.137627

Del Rio Castillo, A. E., Pellegrini, V., Sun, H., Buha, J., Dinh, D. A., Lago, E., et al. (2018). Exfoliation of few-layer black phosphorus in low-boiling-point solvents and its application in Li-ion batteries. *Chem. Mat.* 30, 506–516. doi:10.1021/acs.chemmater.7b04628

Ding, Y., Chen, Y., Xu, N., Lian, X., Li, L., Hu, Y., et al. (2020). Facile synthesis of $FePS_3$ Nanosheets@MXene composite as a high-performance anode. *Material Sodium Storage Nanomicro Lett* 12, 54. doi:10.1007/s40820-020-0381-y

Dunn, B., Kamath, H., and Tarascon, J.-M. (2011). Electrical energy storage for the grid: A battery of choices. *Science* 334, 928–935. doi:10.1126/science.1212741

Duveau, D., Israel, S. S., Fullenwarth, J., Cunin, F., and Monconduit, L. (2016). Pioneer study of SiP_2 as negative electrode for Li and Na-ion batteries. *J. Mat. Chem. A* 4, 3228–3232. doi:10.1039/c6ta00103c

Edison, E., Chaturvedi, A., Ren, H., Sreejith, S., Lim, C. T., and Madhavi, S. (2018). Route of irreversible transformation in layered tin thiophosphite and enhanced lithium storage performance. *ACS Appl. Energy Mat.* 1, 5772–5778. doi:10.1021/acsaem.8b01357

Fan, C.-Y., Zhang, X.-H., Shi, Y.-H., Xu, H.-Y., Zhang, J.-P., and Wu, X.-L. (2019). 2D few-layer iron phosphosulfide: A self-buffer heterophase structure induced by irreversible breakage of P–S bonds for high-performance lithium/sodium storage. *J. Mat. Chem. A* 7, 1529–1538. doi:10.1039/c8ta09057b

Goodenough, J. B. (2014). Electrochemical energy storage in a sustainable modern society. *Energy Environ. Sci.* 7, 14–18. doi:10.1039/c3ee42613k

Gusmão, R., Sofer, Z. K., Sedmidubsky, D., Huber, S. T. P. N., and Pumera, M. (2017). The role of the metal element in layered metal phosphorus triselenides upon their electrochemical sensing and energy applications. *ACS Catal.* 7, 8159–8170. doi:10.1021/acscatal.7b02134

Gusmão, R., Sofer, Z., and Pumera, M. (2019). Metal phosphorous trichalcogenides ($MPCh_3$): From synthesis to contemporary energy challenges. *Angew. Chem. Int. Ed.* 58, 9326–9337. doi:10.1002/anie.201810309

Jana, R., Chowdhury, C., and Datta, A. (2020). Transition-metal phosphorus trisulfides and its vacancy defects: Emergence of a new class of anode material for Li-ion batteries. *ChemSusChem* 13, 3855–3864. doi:10.1002/cssc.202001302

Jiang, H., Chen, B., Pan, J., Li, C., Liu, C., Liu, L., et al. (2017). Strongly coupled FeP@reduced graphene oxide nanocomposites with superior performance for lithium-ion batteries. *J. Alloys Compd.* 728, 328–336. doi:10.1016/j.jallcom.2017.09.021

Kim, M. G., and Cho, J. (2009). Reversible and high-capacity nanostructured electrode materials for Li-ion batteries. *Adv. Funct. Mat.* 19, 1497–1514. doi:10.1002/adfm.200801095

Kong, F., Lv, L., Gu, Y., Tao, S., Jiang, X., Qian, B., et al. (2019). Nano-sized $FeSe_2$ anchored on reduced graphene oxide as a promising anode material for lithium-ion and sodium-ion batteries. *J. Mat. Sci.* 54, 4225–4235. doi:10.1007/s10853-018-3143-1

Latiff, N. M., Mayorga-Martinez, C. C., Khezri, B., Szokolova, K., Sofer, Z., Fisher, A. C., et al. (2018). Cytotoxicity of layered metal phosphorus chalcogenides (MPXY) nanoflakes; $FePS_3$, $CoPS_3$, $NiPS_3$. *FlatChem* 12, 1–9. doi:10.1016/j.flatc.2018.11.003

Li, L., Peng, Y., and Yang, H. (2013). Phase structure changes of MnP anode material during electrochemical lithiation and delithiation process. *Electrochimica Acta* 95, 230–236. doi:10.1016/j.electacta.2013.02.057

Li, N., Zhang, Y., Zhao, H., Liu, Z., Zhang, X., and Du, Y. (2016). Synthesis of high-quality α-MnSe nanostructures with superior lithium storage properties. *Inorg. Chem.* 55, 2765–2770. doi:10.1021/acs.inorgchem.5b02558

Li, W., Li, X., Yu, J., Liao, J., Zhao, B., Huang, L., et al. (2019a). A self-healing layered GeP anode for high-performance Li-ion batteries enabled by low formation energy. *Nano Energy* 61, 594–603. doi:10.1016/j.nanoen.2019.04.080

Li, X., Li, W., Shen, P., Yang, L., Li, Y., Shi, Z., et al. (2019b). Layered GeP-black $P(Ge_2P_3)$: An advanced binary-phase anode for Li/Na-storage. *Ceram. Int.* 45, 15711–15714. doi:10.1016/j.ceramint.2019.04.219

Li, X., Wu, X., and Yang, J. (2014). Half-metallicity in $MnPSe_3$ exfoliated nanosheet with carrier doping. *J. Am. Chem. Soc.* 136, 11065–11069. doi:10.1021/ja505097m

Li, Z., Liu, H., Huang, J., and Zhang, L. (2019c). MOF-derived α-MnSe/C composites as anode materials for Li-ion batteries. *Ceram. Int.* 45, 23765–23771. doi:10.1016/j.ceramint.2019.08.093

Liu, C., Li, F., Ma, L. P., and Cheng, H. M. (2010). Advanced materials for energy storage. *Adv. Mat.* 22, E28–E62. doi:10.1002/adma.200903328

Liu, D.-H., Li, W.-H., Liang, H.-J., Lü, H.-Y., Guo, J.-Z., Wang, J., et al. (2018). Coaxial α-MnSe@ N-doped carbon double nanotubes as superior anode materials in Li/Na-ion half/full batteries. *J. Mat. Chem. A* 6, 15797–15806. doi:10.1039/C8TA03967D

Liu, F., Wang, L., Zhang, Z., Shi, P., Feng, Y., Yao, Y., et al. (2020). A mixed lithium-ion conductive Li_2S/Li_2Se protection layer for stable lithium metal anode. *Adv. Funct. Mat.* 30, 2001607. doi:10.1002/adfm.202001607

Liu, X., Najam, T., Yasin, G., Kumar, M., and Wang, M. (2021). Facile synthesis of MPS_3/C (M= Ni and Sn) hybrid materials and their application in lithium-ion batteries. *ACS omega* 6, 17247–17254. doi:10.1021/acsomega.1c01042

Pei, Q., Wang, X.-C., Zou, J.-J., and Mi, W.-B. (2018). Tunable electronic structure and magnetic coupling in strained two-dimensional semiconductor MnPSe3. *Front. Phys. (Beijing).* 13, 137105–137108. doi:10.1007/s11467-018-0796-9

Ren, X., Zhao, Y., Li, Q., Cheng, F., Wen, W., Zhang, L., et al. (2020). A novel multielement nanocomposite with ultrahigh rate capacity and durable performance for sodium-ion battery anodes. *J. Mat. Chem. A* 8, 11598–11606. doi:10.1039/D0TA04349D

Samal, R., Sanyal, G., Chakraborty, B., and Rout, C. S. (2021). Two-dimensional transition metal phosphorous trichalcogenides (MPX_3): A review on emerging trends, current state and future perspectives. *J. Mat. Chem. A* 9, 2560–2591. doi:10.1039/D0TA09752G

Sang, Y., Wang, L., Cao, X., Ding, G., Ding, Y., Hao, Y., et al. (2020). Emerging 2D-Layered $MnPS_3$/rGO composite as a superior anode for sodium-ion batteries. *J. Alloys Compd.* 831, 154775. doi:10.1016/j.jallcom.2020.154775

Shen, H., Huang, Y., Hao, R., Chang, Y., Ma, Z., Guo, B., et al. (2020). Mechanical robustness two-dimensional silicon phosphide flake anodes for lithium ion batteries. *ACS Sustain. Chem. Eng.* 8, 17597–17605. doi:10.1021/acssuschemeng.0c07441

Tang, H., Lu, X., Zhu, H., Tian, Y., Khatoon, R., Zhu, Z., et al. (2020). Hydrothermally synthesized MnSe as high cycle stability anode material for lithium-ion battery. *Ionics* 26, 43–49. doi:10.1007/s11581-019-03180-5

Wang, F., Shifa, T. A., Yu, P., He, P., Liu, Y., Wang, F., et al. (2018). New Frontiers on van der Waals layered metal phosphorous trichalcogenides. *Adv. Funct. Mat.* 28, 1802151. doi:10.1002/adfm.201802151

Xing, S., Yang, J., Wang, C., Zhou, J., Zhang, J., Zhang, L., et al. (2020). Fabrication of van der Waals heterostructured $FePSe_3$/carbon hybrid nanosheets for sodium storage with high performance. *ACS Appl. Mat. Interfaces* 12, 54732–54741. doi:10.1021/acsami.0c16396

Xu, Z., Huang, Y., Chen, C., Ding, L., Zhu, Y., Zhang, Z., et al. (2020). MOF-derived hollow Co (Ni) Se_2/N-doped carbon composite material for preparation of sodium ion battery anode. *Ceram. Int.* 46, 4532–4542. doi:10.1016/j.ceramint.2019.10.181

Xue, M.-Z., and Fu, Z.-W. (2007). Manganese selenide thin films as anode material for lithium-ion batteries. *Solid State Ionics* 178, 273–279. doi:10.1016/j.ssi.2006.12.020

Yousaf, M., Wang, Z., Wang, Y., Chen, Y., Ali, U., Maqbool, M., et al. (2020). Core–shell $FeSe_2$/C nanostructures embedded in a carbon framework as a free standing anode for a sodium ion battery. *Small* 16, 2002200. doi:10.1002/smll.202002200

Yu, N., Zou, L., Li, C., and Guo, K. (2019a). *In-situ* growth of binder-free hierarchical carbon coated $CoSe_2$ as a high performance lithium ion battery anode. *Appl. Surf. Sci.* 483, 85–90. doi:10.1016/j.apsusc.2019.03.258

Yu, Z., Peng, J., Liu, Y., Liu, W., Liu, H., and Guo, Y. (2019b). Amine-assisted exfoliation and electrical conductivity modulation toward few-layer $FePS_3$ nanosheets for efficient hydrogen evolution. *J. Mat. Chem. A* 7, 13928–13934. doi:10.1039/C9TA03256H

Zhang, S., Guo, S., Huang, Y., Zhu, Z., Cai, B., Xie, M., et al. (2016). Two-dimensional SiP: An unexplored direct band-gap semiconductor. *2D Mat.* 4, 015030. doi:10.1088/2053-1583/4/1/015030